

Satellite-Based Operational Solar Irradiance Forecast for Uruguay’s Solar Power Plants

Rodrigo Alonso-Suárez*, Franco Marchesoni, Liber Dovat and Agustín Laguarda
Laboratorio de Energía Solar (LES, <http://les.edu.uy/>), Facultad de Ingeniería, Universidad de la República
*E-mail: r.alonso.suarez@gmail.com

Abstract—This work presents and validates an intra-day operational solar forecast for the southern cone of South America based on GOES16 satellite images. The forecast is evaluated over 12 photovoltaic (PV) generation sites in the northwest of Uruguay. The irradiance predictions are obtained from the combination of different satellite cloudiness forecasts and a standard satellite-to-irradiance conversion model, both specifically adapted to the region. The core of the system is a Cloud Motion Vector (CMV) satellite technique, considered in different spatial resolutions. The optimal linear combination of a single-pixel and space-averaged CMV forecast with the space-averaged persistence is proposed and analyzed. The performance assessment of the individual sub-forecasts and their combination is presented for each time horizon between 10 minutes and 4 hours, with a 10 minutes time step.

Index Terms—solar forecast, CMV, GOES16 satellite, GHI.

I. INTRODUCTION

The short-term variability of non-conventional renewable energy resources such as wind and solar introduces uncertainty in the electricity dispatch. The solar resource is known for its high temporal and spatial variability, caused by passing and forming clouds. As a consequence, the large integration of solar energy to electricity grids poses a major challenge for grid operators [1]. Mitigation actions can be introduced to deal with the resource intermittency, including storage solutions, spatial distribution of the variable generators and resource prediction. Solar resource forecasting provides an informed decision-making framework, allowing to optimally manage the generators (unit commitment) and system reserves, reducing the operational costs associated with the service’s quality and continuity, and lowering the uncertainty in the electricity market transactions [2] both in availability and price.

Solar predictions can be obtained by different means depending on the time horizon and spatial domain [3]. There mainly exist four families of methods that cover the practical uses, namely, numerical weather predictions (NWP), satellite nowcast, ground-based sky images and statistical tools, i.e. machine learning techniques. NWP allow to forecast hourly irradiation up to several days ahead [5, 6, 7] with global and regional coverage and varying spatial resolution depending on the computational resources, typically above 10 km. On the other side of the solar forecasting spectrum, ground-based cameras allow to forecast 1-minute irradiance with high spatial resolution (at plant level) up to $\simeq 30$ minutes ahead [8, 9]. Satellite-based solar forecasting strategies account for the intra-day time horizons with $\simeq 1$ km spatial resolution [10, 11, 12]. They are typically used for hourly forecast, but can be applied

in any sub-hourly time granularity, for instance, 30-minutes, 10-minutes and so on. This technique outperforms NWP up to 4 hours ahead [13, 14], and is included in solar forecasting systems of specialized data-providing companies. Finally, the applicability of machine learning approaches critically depends on their input variables, being able to act as a standalone forecasting methodology by means of learning the historic data behavior, as a post-processing technique by using ground measured data or as a forecast integration tool, combining different prediction sources.

In this work we build and evaluate an operational satellite forecasting tool to predict solar global horizontal 10-minutes irradiance (GHI) for Uruguay’s territory up to 4 hours ahead with a refresh rate of 10-minutes. The system is based on the cloudiness motion estimation from visible channel geostationary satellite images. These kind of techniques are known as CMV methods. The motion field is then used to predict the future position of clouds, i.e. the future images, from where a solar irradiance prediction can be produced by using standard satellite-to-irradiance estimation models. The cloudiness prediction developed here linearly combines three sub-forecast’s outputs: (i) single-pixel CMV prediction, (ii) space-averaged CMV prediction and (iii) space-averaged persistence. Each sub-forecast and their combination are assessed at cloudiness and GHI levels, showing that this simple combination strategy success to outperform each individual forecast. We provide the combination weights to be used for the region, specially tuned for Uruguay’s photovoltaic (PV) power plants’ locations, and show that a regionally-tuned combination is enough for optimal performance, being of little value to optimize the combination for each individual location. The operational version of the forecast system is evaluated (<http://les.edu.uy/online/pronostico.php>), thus addressing some inherent imperfections of the real-time operation, such as the asynchronous image reception and data gaps due to satellite maintenance, among others. This is the first work that implements and evaluates these kind of solar forecasting techniques with the GOES16 satellite’s imagery in the region.

This work is organized as follows. Section II describes the satellite data being used and the PV plants’ locations, for which the predictions’ combination is adjusted. Section III presents the forecasts methods and Section IV defines the evaluation framework. The performance results and analysis of the system are presented in Section V. Finally, Section VI summarizes our conclusions.

II. DATA

This work requires only visible channel geostationary satellite images. Uruguay’s region is best covered by the GOES-East meteorological satellite (GOES16) of the National Oceanic and Atmospheric Administration (NOAA, USA). The images are publicly available and distributed via different broadcasting systems, including satellite communications and internet. The image’s rate is of 10 minutes and their space resolution at the satellite nadir is of 500 m. The space resolution is variable across the image, being of $\simeq 1$ km in our region. Both the space and time resolution of this satellite’s images are adequate to model a highly fluctuating phenomena like solar radiation. The outgoing radiance measured by the satellite’s visible channel is typically converted to planetary reflectance (ρ), which is a proxy for cloudiness, as clouds reflect more solar radiation to outer space than the typical soil backgrounds (excluding for instance snowy areas or salt flats, not present in the region of study). The cloudiness level is then represented by ρ . Furthermore, clouds are the only moving object in the images’ sequence, so subsequent images can be used directly to estimate the clouds’ motion.

Satellite solar assessment models convert the ρ images into solar irradiance images. Different models are available for the different solar irradiance components. In this work we use the locally adjusted CIM-ESRA model [15] for GHI estimation. This model is used to produce the solar irradiance forecast from the cloudiness (ρ) predictions, and also to generate the GHI ground truth to assess the forecast. In light of the high uncertainty of current solar forecasts, it has been demonstrated that solar satellite estimations can be used as reference for the performance evaluation [16].

This work is done with three months (April to June 2021) of operational solar forecast provided by the Solar Energy Laboratory (LES, <http://les.edu.uy/>). Although the CMV forecast is produced for all the satellite’s image span, including Uruguay, Argentina, Paraguay, Chile, south Brazil and south Bolivia, the forecast will be evaluated at Uruguay’s PV power plants locations, showed in Table I. These sites correspond to the northwest of Uruguay, a subtropical temperate region with intermediate solar irradiance variability [17], where the highest solar resource of the country is available [18]. The ‘bdo’ site groups six individual PV power plants (P05-P10) which are located very close (in a radius of less than 1 km). The aggregate of these sites is considered as a single location to avoid geographical over-representation, in particular, in the combination algorithm’s training.

III. FORECASTING METHODS

The CMV technique used here is the Farneback optical flow algorithm [19], which allows a dense motion estimation between two consecutive images. This method is based on a second order polynomial expansion of each pixel’s neighbourhood that is introduced to deal with noisy sequences, providing smoother CMV estimations. This is an interesting choice as satellite images are prone to noise in the signal processing sense [11]. The algorithm is implemented

TABLE I
INFORMATION OF THE PV POWER PLANTS

station name	station code	lat. (deg)	lon. (deg)	Power (MW)
ASAHI	P01	-31.2807	-57.9171	0.5
La Jacinta	P02	-31.4321	-57.9084	50.0
Alto Cielo	P03	-30.4214	-57.4608	20.0
Raditon	P04	-32.3871	-58.1328	8.0
Naranjal	P11	-31.2627	-57.8709	50.0
Del Litoral	P12	-31.4407	-57.8643	16.0
Menafra Solar	P13	-32.6079	-57.4372	20.0
Arapey Solar	P14	-30.8734	-57.4543	10.0
Natelu	P15	-33.2617	-57.9917	9.5
Yarnel	P16	-32.6860	-57.6066	9.5
Casalko	P17	-32.2096	-58.0050	1.8
Bola de Oro	bdo	-32.2916	-58.0260	33.3

in our operational forecast with the `CALCOPTICALFLOW-FARNEBACK` function of the Python `OpenCV 3.x` libraries with the parameters of Table II. These parameters include the window length, the down-scaling levels and configuration, and some specifications for the polynomial expansion implementation. More information about these parameters can be found in the method’s `OpenCV` documentation. The values of Table II resulted from a preliminary optimization done by our team over a reduced set of images.

TABLE II
PARAMETERS USED FOR THE FARNEBÄCK OPTICAL FLOW METHOD

parameter	value	parameter	value
winsize	22 pixels	poly_n	5
levels	4	poly_sigma	0.848
pyr_scale	0.39872	iterations	3

The future position of clouds is predicted by extrapolating the image’s motion. The extrapolation is the standard backward search, in which the next image is constructed by setting $\rho(x, y, t + 1) = \rho(x - u, y - v, t)$, where (u, v) is the CMV estimation, (x, y) is the spatial domain and t is the time (in this work each time step represents 10 minutes). The following predicted images, $\rho(x, y, t + h)$ with h up to 24 (corresponding to 240 minutes, namely, 4 hours), are generated in a recursive way by using the CMV and the previous prediction, initiating with the image at time t . This procedure is repeated every 10-minutes when each new received image is available and is illustrated in Fig. 1.

The images’ predictions can be considered at an instantaneous single-pixel level (each PV plant is a single pixel) or averaged over a close neighbourhood (spatial smoothing of 10×10 pixels), which better represent the 10-minutes average conditions via an ergodic assumption [15]. As it will be shown in Section V, the single-pixel CMV method

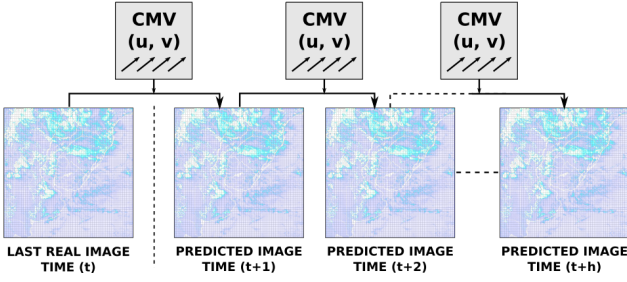


Fig. 1. Iterative procedure to predict the future images using the CMV and the last received image (last available real image). The procedure is done at cloudiness level (ρ).

is best performing for the shorter lead times while the space-averaged CMV is best for the larger ones. This suggest to combine them depending on the forecast horizon. Another information that can be considered for the combination is the persistence of the ρ image, both at single-pixel and space-averaged levels. The common persistence (in this case, the single-pixel approach) is usually difficult to outperform in the shorter lead times [20] by more sophisticated forecasting techniques (i.e. for intra-hour forecast). However, the joint use of the single-pixel CMV and single-pixel persistence lead to almost no performance change and, being the single-pixel CMV best performing, we found no point in including the single-pixel persistence in the combination. On the other hand, the space-averaged persistence did provide an added value to the combination, hence it is included in the current operational system. This sub-forecast combination is done at cloudiness level (ρ), as a linear combination with weights w_i . The weights are then enforced to depend on the forecast horizon h and to satisfy $\sum_i w_i(h) = 1$ for each h . The combined solar forecasting system is illustrated in Fig. 2, including the GHI conversion with the CIM-ESRA model.

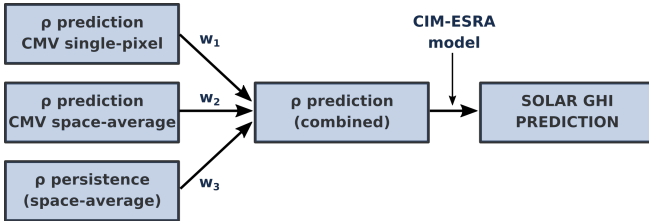


Fig. 2. Forecast combination strategy.

IV. EVALUATION FRAMEWORK

To quantify the performance of the predicted series of ρ and GHI in each site, the mean bias deviation (MBD) and the root mean square deviation (RMSD) are used. These similarity metrics are defined as:

$$\text{MBD} = \frac{1}{N} \sum_i (\hat{y}_i - y_i), \quad \text{RMSD} = \sqrt{\frac{1}{N} \sum_i (\hat{y}_i - y_i)^2},$$

where \hat{y}_i correspond to the predicted series and y_i to the reference data series [21]. These quantities can be also expressed as a percentage of the mean of the reference data (metric's relative values). For ρ , the predictions are compared

with the satellite images directly, while for GHI the reference data series are obtained with the CIM-ESRA model.

To assess the gain of the different forecasting methods, the persistence benchmark is used. The persistence method in this case is to maintain constant ρ for all the lead times, i.e. $\rho(x, y, t + h) = \rho(x, y, t) \forall h$. This constant ρ is then used for the GHI persistence via the CIM-ESRA model. Note that a constant ρ does not imply constant GHI, being the selected procedure a more exigent solar irradiance performance benchmark than the prior.

V. RESULTS

For the sake of clarity and brevity the hereafter discussion will be presented by tables that contain some of the forecast horizons in the whole $h = 1 \dots 24$ span and figures. The full data for all time horizons, including the operational weights and the complete set of evaluation metrics, is provided to the reader in http://les.edu.uy/RDpub/UY_solar_forecast.ods.

The sub-forecasts combination is determined by the weights of the linear regression for each time horizon, $w_i(h)$. Their evolution with the forecast horizon is illustrated in Fig. 3 and shown in Table III. It is observed that the single-pixel CMV has a higher weight (w_1) for the shorter time horizons. Then, its value drops almost to zero at $\simeq 70$ minutes (6-8 lead times). The space-averaged CMV becomes more relevant (w_2) for intermediate forecast horizons, reaching its highest weights at 60-70 minutes ahead and remaining the most relevant for the majority of lead times. On the other hand, the performance of the space-averaged persistence method is increasingly important with the time horizon, being almost equal to the space-averaged CMV for the larger lead times (the last hour and a half of forecast, in which $w_2 \approx w_3 \approx 0.5$).

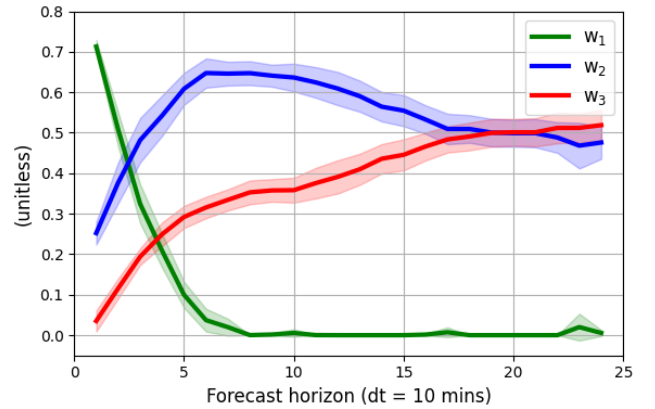


Fig. 3. Weights vs forecast horizon, averaged over all sites (solid lines). The shadow-bands represent one standard deviation between sites.

Fig. 4 shows the average relative RMSD over the sites of Table I for all the forecasts methods and their combination, at cloudiness level (ρ). As expected, the uncertainty increases with the lead times. The single-pixel persistence is included as a reference, and it is outperformed by all other methods. The combined method achieves the best performance, and is analyzed here in two manners: by using the specific weights for each site (local) or by using the average weights

TABLE III
AVERAGE WEIGHTS TO BE USED IN THE REGION

lead time	w_1	w_2	w_3
10 mins	0.713	0.252	0.035
20 mins	0.508	0.377	0.116
30 mins	0.324	0.482	0.194
40 mins	0.209	0.542	0.249
50 mins	0.100	0.608	0.292
60 mins	0.037	0.647	0.315
90 mins	0.002	0.641	0.357
120 mins	0.000	0.609	0.391
150 mins	0.000	0.555	0.445
180 mins	0.000	0.509	0.491
210 mins	0.000	0.499	0.501
240 mins	0.005	0.476	0.519

across sites (regional). The performance of both combination approaches is almost the same, overlapping in Fig. 4. This means that the regional weights are enough to achieve almost the best performance of the linear combination method and that there is little value in fine-tuning the weights for each site. The conclusions at GHI level are almost the same, as shown in Fig. 5. The only minor difference is that the single-pixel CMV method almost matches the performance of single-pixel persistence for the last lead times, which for instance is not relevant for the combination as $w_1 \approx 0$ for these forecast horizons. As observed by comparing both figures, the uncertainty for GHI prediction is lower than for ρ prediction.

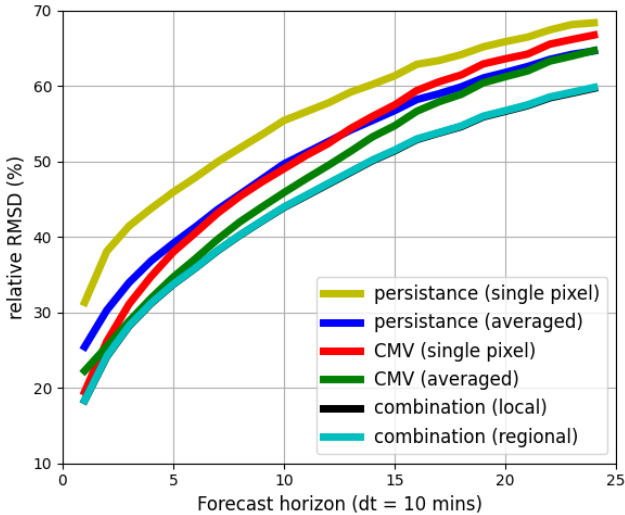


Fig. 4. Performance assessment at cloudiness level (ρ).

Regarding the average relative MBD (over sites) all methods exhibit a similar behavior. This claim is illustrated in Fig. 6. This figure shows the all-methods' average trend with the forecast horizon along with one standard deviation

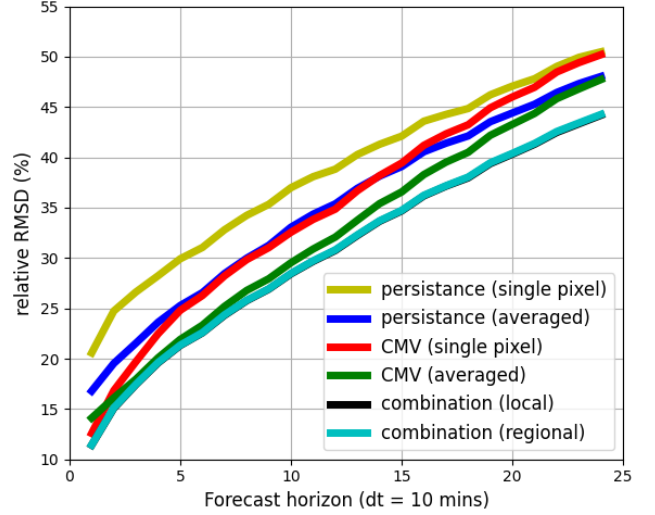


Fig. 5. Performance assessment at solar irradiance level (GHI).

of the methods' performance in shadow-bands, for both cloudiness (blue) and irradiance (red) forecasts. As seen in the figure, the inter-model standard deviation is low for both curves, meaning that all models introduce similar bias at each forecast horizon. Each model's average relative MBD is provided in the full data spreadsheet, where the same conclusion can be derived. An opposite MBD trend is observed for cloudiness and irradiance forecasts, as is easily distinguished in Fig. 6. While cloudiness is overestimated for the shorter lead times and underestimated for the larger ones, the opposite occurs for solar irradiance. This behavior is naturally understood as the occurrence of clouds is negatively correlated with solar irradiance: if clouds are overestimated then solar irradiance is underestimated, and viceversa. The relative bias introduced in the solar irradiance forecast is slightly lower than for cloudiness, with a span of 5.7% (GHI interval $[-0.4\%; +5.3\%]$), in comparison with the span of 7.7% of the latter (ρ interval $[+0.5\%; -7.2\%]$).

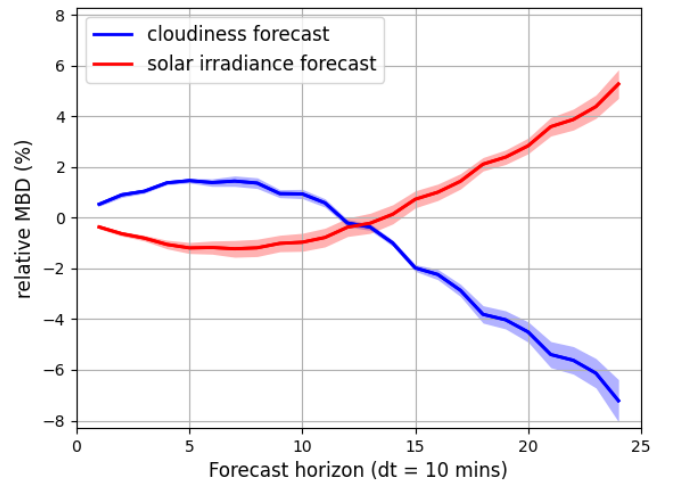


Fig. 6. Relative MBD as a function of the forecast horizon. The solid line represents the all models average while the shadow-bands represent one standard deviation between models.

TABLE IV
PERFORMANCE METRICS FOR CLOUDINESS FORECAST

lead time	all models MBD (%)		RMSD (%)					
	average value	standard deviation	persistence single pixel	persistence averaged	CMV single pixel	CMV averaged	local combination	regional combination
10 mins	+0.5	0.1	25.4	19.5	22.3	31.3	18.3	18.4
20 mins	+0.9	0.1	30.3	26.1	25.5	38.1	24.1	24.2
30 mins	+1.0	0.1	33.9	31.1	28.8	41.4	28.2	28.2
40 mins	+1.4	0.1	36.8	34.8	31.9	43.8	31.2	31.2
50 mins	+1.5	0.1	39.1	38.0	34.7	45.9	33.7	33.7
60 mins	+1.4	0.1	41.3	40.5	37.1	47.9	35.9	35.9
90 mins	+1.0	0.2	47.6	47.3	43.9	53.5	42.1	42.1
120 mins	-0.2	0.1	52.6	52.3	49.5	57.7	47.0	47.1
150 mins	-2.0	0.1	56.7	57.5	54.7	61.3	51.4	51.5
180 mins	-3.8	0.3	59.9	61.4	58.9	64.1	54.6	54.7
210 mins	-5.4	0.5	62.5	64.2	62.0	66.4	57.4	57.5
240 mins	-7.2	0.8	64.6	66.7	64.7	68.3	59.7	59.8

TABLE V
PERFORMANCE METRICS FOR SOLAR IRRADIANCE FORECAST

lead time	all models MBD (%)		RMSD (%)					
	average value	standard deviation	persistence single pixel	persistence averaged	CMV single pixel	CMV averaged	local combination	regional combination
10 mins	-0.4	0.1	16.8	12.6	14.1	20.6	11.4	11.4
20 mins	-0.6	0.1	19.5	16.8	16.1	24.7	15.1	15.1
30 mins	-0.8	0.1	21.5	19.7	18.0	26.6	17.4	17.5
40 mins	-1.1	0.2	23.6	22.5	20.1	28.2	19.6	19.6
50 mins	-1.2	0.2	25.3	24.8	21.9	29.9	21.3	21.3
60 mins	-1.2	0.3	26.6	26.3	23.3	31.0	22.6	22.6
90 mins	-1.0	0.3	31.3	31.0	27.9	35.3	26.9	26.9
120 mins	-0.4	0.4	35.4	34.9	32.1	38.8	30.7	30.8
150 mins	+0.7	0.3	39.1	39.4	36.6	42.1	34.7	34.7
180 mins	+2.1	0.3	42.1	43.2	40.5	44.8	38.0	38.0
210 mins	+3.6	0.4	45.3	47.0	44.4	47.8	41.3	41.4
240 mins	+5.3	0.6	48.0	50.2	47.7	50.5	44.2	44.3

Tables IV and V provide the quantitative values of relative MBD and RMSD for all considered methods averaged over all sites and for some representative forecast horizons. In the case of the relative MBD, the all-models average and standard deviation are provided. Full results for these metrics for all methods and forecast horizons are provided in the full data spreadsheet, as mentioned before.

VI. CONCLUSION

A solar forecasting system was developed for the southern cone of South America based on a satellite CMV technique. This system is able to provide intra-day cloudiness and surface global horizontal irradiance (GHI) predictions up to 4 hours ahead with 10-minutes time steps based on GOES16 imagery. The forecast is evaluated for 3 months over the PV Power plants' location in Uruguay (12 sites). The most accurate method from the ones inspected here is the linear combination of three inputs: a single-pixel

CMV forecast, a space-averaged CMV forecast and a space-averaged persistence procedure. The weighting parameters are robust and not strongly site dependent, so a unique set of values can be used for all stations. The bias introduced by each method has a similar trend with the forecast horizon, and is slightly lower (in absolute terms) for solar irradiance forecast than for cloudiness forecast, having both opposite overestimation/underestimation behavior. The described algorithm is currently providing operational forecast for these PV sites in Uruguay with a 10-minutes refresh rate, but can be upgraded to provide solar forecast at any site in the region.

ACKNOWLEDGMENT

The authors would like to acknowledge that this work was done under a funded agreement with Uruguay's Administración del Mercado Eléctrico (ADME, <https://adme.com.uy/>).

REFERENCES

- [1] C. Voyant, G. Notton, S. Kalogirou, M.L. Nivet, C. Paoli, F. Motte, A. Fouilloy, *Machine learning methods for solar radiation forecasting: A review*. *Renewable Energy* 105:569-582, 2017.
- [2] J. Antonanzas, N. Osorio, R. Escobar, R. Urraca, F.J. Martinez-de-Pison, F. Antonanzas-Torres, *Review of photovoltaic power forecasting*. *Solar Energy* 136:78-111, 2016.
- [3] M. Diagne, M. David, P. Lauret, J. Boland, N. Schmutz, *Review of solar irradiance forecasting methods and a proposition for small-scale insular grids*. *Renewable and Sustainable Energy Reviews* 27:65-76, 2013.
- [4] R. Perez, S. Kivalov, J. Schlemmer, K. Hemker, D. Renee, T. Hoff, *Validation of short and medium term operational solar radiation forecast in the US*. *Solar Energy* 84:2161-2172, 2010.
- [5] R. Perez, E. Lorenz, S. Pelland, M. Beauharnois, G. Van Knowe, K. Hemker, D. Heinemann, J. Remund, S.C. Müller, W. Traunmüller, G. Steinmauer, D. Pozo, J.A. Ruiz-Arias, V. Lara-Fanego, L. Ramirez-Santigosa, M. Gaston-Romero, L.M. Pomares, *Comparison of numerical weather prediction solar irradiance forecasts in the US, Canada and Europe*. *Solar Energy* 94:305-326, 2013.
- [6] P. Mathiesen, J. Kleissl, *Evaluation of numerical weather prediction for intra-day solar forecasting in the continental United States*. *Solar Energy* 85(5):967-977, 2011.
- [7] V. Lara-Fanego, J.A. Ruiz-Arias, D. Pozo-Vázquez, F.J. Santos-Alamillos, J. Tovar-Pescador, *Evaluation of the WRF model solar irradiance forecasts in Andalusia (southern Spain)*. *Solar Energy* 86(8):2200-2217, 2012.
- [8] C.W. Chow, B. Urquhart, M. Lave, A. Dominguez, J. Kleissl, J. Shields, B. Washom, *Intra-hour forecasting with a total sky imager at the UC San Diego solar energy testbed*. *Solar Energy* 85(11):2881-2893, 2011.
- [9] M. Caldas, R. Alonso-Suárez, *Very short-term solar irradiance forecast using all-sky imaging and real-time irradiance measurements*. *Renewable Energy* 143:1643-1658, 2019.
- [10] E. Lorenz, A. Hammer, D. Heinemann, *Short term forecasting of solar radiation based on satellite data*. *Proceedings of the EUROSUN2004 (ISES European Solar Congress)*, pp. 841-848, 2004.
- [11] Z. Peng, S. Yoo, D. Yu, D. Huang, *Solar irradiance forecast system based on geostationary satellite*. *Proceedings of the 2013 IEEE International Conference on Smart Grid Communications (SmartGridComm)*, pp. 708-713, 2013.
- [12] G. Giacosa, R. Alonso-Suárez, *Performance assessment of intra-day solar irradiation forecast in Uruguay using satellite cloud motion vectors*. *Proceedings of the ISES Solar World Congress*, 2019.
- [13] R. Perez, T.E. Hoff, *Chapter 10 - SolarAnywhere Forecasting*. In *Solar Energy Forecasting and Resource Assessment*, Ed.: Jan Kleissl, Academic Press, 233-265, 2013.
- [14] J. Kühnert, E. Lorenz, D. Heinemann, *Chapter 11 - Satellite-Based Irradiance and Power Forecasting for the German Energy Market*. In *Solar Energy Forecasting and Resource Assessment*, Ed.: Jan Kleissl, Academic Press, 267-297, 2013.
- [15] A. Laguarda, G. Giacosa, R. Alonso-Suárez, G. Abal, *Performance of the site-adapted CAMS database and locally adjusted cloud index models for estimating global solar horizontal irradiation over the Pampa Húmeda*. *Solar Energy* 199:295-307, 2020.
- [16] D. Yang, R. Perez, *Can we gauge forecasts using satellite-derived solar irradiance?* *Journal of Renewable and Sustainable Energy* 11, 023704, 2019.
- [17] F. Marchesoni-Acland, R. Alonso-Suárez, *Intra-day solar irradiation forecast using RLS filters and satellite images*. *Renewable Energy* 161:1140-1154, 2020.
- [18] R. Alonso-Suárez, G. Abal, P. Musé, R. Siri, *Satellite-derived Solar Irradiation Map for Uruguay*. *Energy Procedia* 57:1237-1246, 2014.
- [19] G. Farnebäck, *Two-Frame Motion Estimation Based on Polynomial Expansion*. In: Bigun J., Gustavsson T. (eds) *Image Analysis*. SCIA 2003. *Lecture Notes in Computer Science*, vol 2749. Springer, Berlin, Heidelberg.
- [20] I. Jolliffe, D. Stephenson, *Forecast Verification. A practitioner's guide in atmospheric science*. John Wiley and Sons, Ltd, London, 2nd edition, 2003.
- [21] G. Giacosa, R. Alonso-Suárez, *Desempeño de la persistencia para la predicción del recurso solar en Uruguay*. *Revista Brasileira de Energía Solar* 9(2):107-116, 2018.